Journal of the Korean Physical Society, Vol. 77, No. 5, September 2020, pp. 388∼394

# Beam Loss Studies at the High Energy Beamlines of the RAON Accelerator

Hyunchang Jin,* Ji-Ho Jang and Dong-O Jeon
*Rare Isotope Science Project, Institute for Basic Science, Daejeon 34000, Korea*

(Received 8 January 2020; revised 25 February 2020; accepted 6 March 2020)

The RAON accelerator is currently under construction to generate and accelerate stable ions and rare isotopes for various kinds of scientific programs, and it will be completed by the end of 2021. In the RAON accelerator, the beams generated by using ion sources such as electron cyclotron resonance ion source and isotope separation on-line can be used in high energy experiments such as a beam irradiation system and a muon spin rotation/relaxation/resonance system after having been accelerated by low energy and high energy superconducting linacs. After the high energy superconducting linac, the beam passes through the high energy beamline and then collides with the target. In 2015, the lattices of the high energy beamlines were designed achromatically to minimize the emittance growth. However, as the specification of magnets in the beamline was changed after first lattice design, a beam dynamics simulation has been performed newly, and beam loss studies have also been conducted. Here, we will present the simulation results for the beam dynamics and describe the beam loss studies performed on the high energy beamlines of the RAON accelerator.

Keywords: RAON accelerator, Beam dynamics, Beam loss
DOI: 10.3938/jkps.77.388

## I. INTRODUCTION

The RAON accelerator has been constructed to provide stable ions and rare isotopes for various scientific programs such as nuclear physics, particle physics, biomedical science, and so on [1]. The beams generated by the isotope separation on-line (ISOL) and the electron cyclotron resonance ion source (ECR-IS) are accelerated through the low-energy and the high-energy linear accelerator sections (SCL1, SCL2, SCL3) consisting of superconducting RF cavities and are transmitted to the target in the experimental hall after having passed through the beamlines. The layout of the RAON accelerator is shown in Fig. 1. The RAON accelerator is currently under construction with the goal of being completed by the end of 2021. By next year, the low-energy accelerator equipment will be installed, after which the high-energy accelerator equipment will be installed at the tunnel. In addition, the beam commissioning at the injector section will start next year, and the beam commissioning at the superconducting linac will be continued according to the equipment installation schedule.

While the development of the accelerator equipment is in progress, the lattice design and the beam dynamics studies have been also carried out for the RAON accelerator [2, 3], and each beamline to the experimental halls was also designed as satisfying the target requirement in 2015 [4,5]. Among the beamlines, there are two beamlines to high energy experimental hall; one is the beamline to the beam irradiation system (BIS), and the other is the beamline to the muon spin relaxation / resonance (muSR or $\mu$SR) system. Recently, as the beam pipe size of the quadrupole was adjusted from 4.0 cm to 3.2 cm, the beam stability needs to be identified newly. For this reason, the beam optics has been calculated to decrease the beam size for each beamline by using the ELEGANT code [6]. Also, the particle tracking simulations and beam loss studies were carried out carefully by using the TRACK code [7].

## II. BIS BEAMLINE

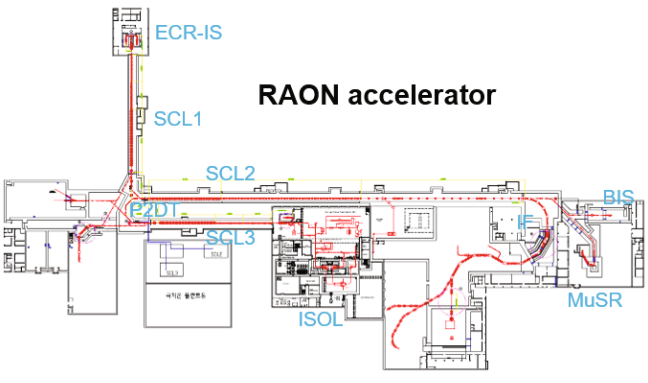


Fig. 1. Layout of the RAON accelerator.

*E-mail: hcjin@ibs.re.kr

 

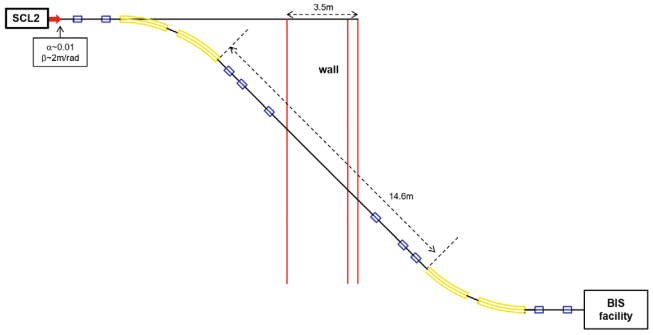


Fig. 2. Layout of the BIS beamline.

Table 1. Carbon beam parameters at the BIS beamline simulations.

| Characteristic | Value | Unit |
|---|---|---|
| Energy | 430 | MeV/u |
| Magnetic rigidity | 6.6 | Tm |
| Velocity in unit of c | 0.729 | - |
| $\varepsilon_{x,rms,norm.}$ | 0.19 | mm.mrad |
| $\varepsilon_{y,rms,norm.}$ | 0.19 | mm.mrad |
| $\beta_{x,y,0}$ | 2.0 | m |
| $\alpha_{x,y,0}$ | 0.01 | - |
| Energy spread | 0.3 | % |
| Beam distribution | 6D water-bag | - |
| Number of macro-particles | 100k | - |

### 1. Beam dynamics simulation

Figure 2 shows the layout of the BIS beamline. The positions of the magnets were determined in 2015 by considering the building wall, and the field strength was also calculated. There are 10 quadrupoles and 4 dipoles, and the lattice is designed with mirror symmetry. Recently, however, the beam pipe size was newly adjusted from 4.0 cm to 3.2 cm, so a beam optics calculation is necessary for beam stability. The carbon beam, $^{12}C^{6+}$, is used as a reference beam at the BIS beamline, and the beam parameters used for following simulations are listed in Table 1.

If the horizontal beam size is to be decreased, the horizontal dispersion should be reduced. The horizontal and vertical dispersion functions are shown in Fig. 4. The maximum value of the horizontal dispersion is decreased, and the vertical one is kept at zero, satisfying the achromatic condition.

Figure 3 shows the beta functions along the BIS beamline, as calculated by using the ELEGANT code. Compared to the results in 2015, the maximum vertical beta functions are reduced significantly. The maximum value of the horizontal beta function was small enough, so those values are almost same.

After the beam optics calculation, the particle tracking simulation was carried out by using 100,000 macro-

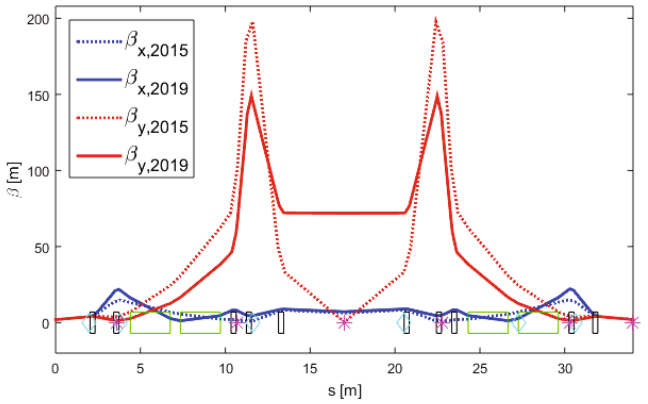


Fig. 3. Beta functions along the BIS beamline. In the figure, a green box, a black box, a cyan diamond, and a magenta star mean a dipole, a quadrupole, a corrector, and a BPM, respectively.

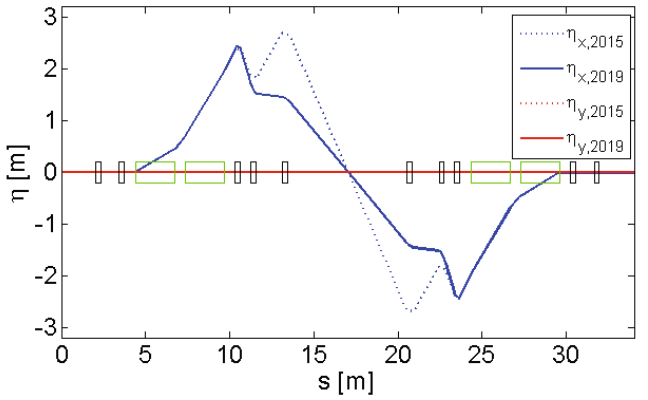


Fig. 4. Dispersion functions along the BIS beamline.

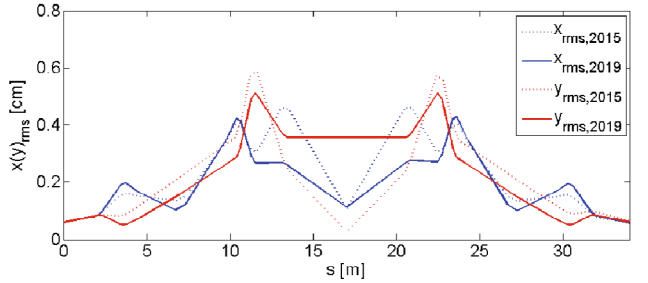


Fig. 5. Transverse rms. beam size obtained using the TRACK code at the BIS beamline.

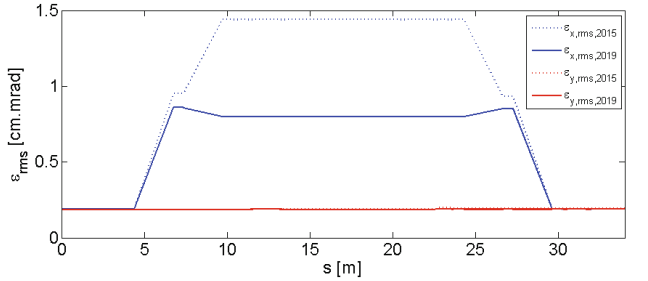


Fig. 6. Transverse rms. emittance obtained using the TRACK code at the BIS beamline.

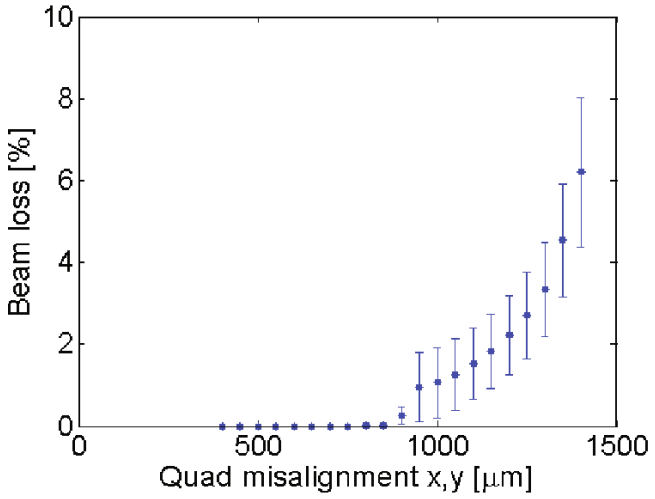


Fig. 7. Average beam loss percentage vs. quadrupole transverse misalignment error for 100 random seeds.

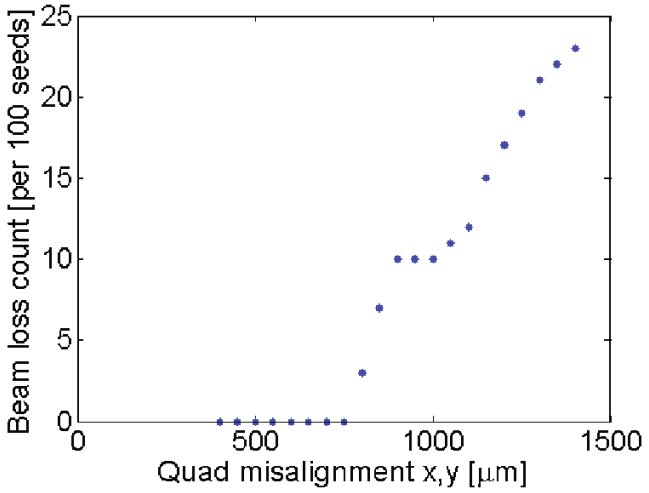


Fig. 8. Beam loss count vs. quadrupole transverse misalignment error for 100 random seeds.

particles with the TRACK code. Figure 5 shows the transverse root-mean-square (rms.) beam size, and the transverse rms. emittance is shown in Fig. 6. The maximum value of the beam size was decreased after the new calculation, and the horizontal emittance was also decreased at the dispersion section.

### 2. Beam loss simulation

Many kinds of machine errors can cause orbit distortion. Among them, transverse misalignment of a quadrupole is a dominant source. The kick, $\Delta\theta$, caused by a quadrupole transverse misalignment is given by

$$\Delta\theta = KL\Delta m, \quad (1)$$

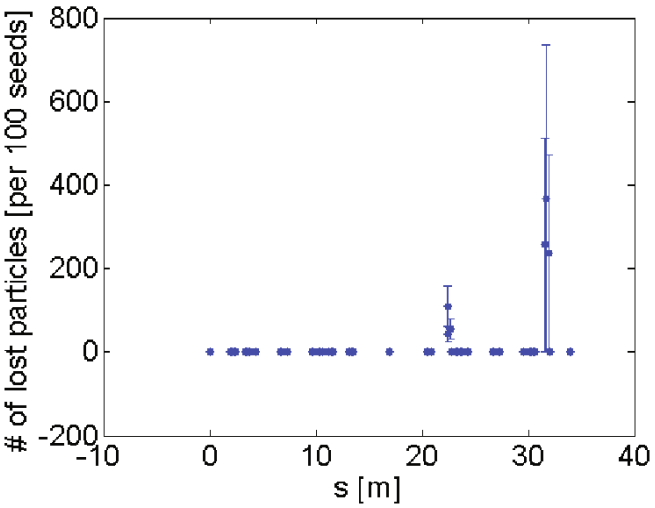


Fig. 9. Beam loss along the BIS beamline for a transverse quadrupole misalignment of 1.0 mm for 100 random seeds.

Table 2. Error tolerance at the BIS beamline.

| Error tolerance | Value | Unit |
|---|---|---|
| Launch error x(y) | ±1.1 (±0.2) | cm |
| Launch error $x_p$ ($y_p$) | ±4.4 (±1.6) | mrad |
| Quadrupole misalignment x,y | ±0.8 | cm |
| Quadrupole misalignment z | ±1.8 | cm |
| Quadrupole tilt | ±3.8 | mrad |
| Dipole misalignment x,y | ±1.3 | cm |
| Dipole tilt | ±1.9 | mrad |

where $K$ is the quadrupole strength, $L$ is the quadrupole length, and $\Delta m$ is the transverse displacement of a quadrupole. For that reason, the orbit distortion was simulated for varying quadrupole transverse misalignment. The magnet error used for the simulations has a uniform distribution and a peak-to-peak type error.

Figure 7 shows the beam loss percentage for the quadrupole transverse misalignment with 100 random seeds. We used 100,000 macro-particles, and one macro-particle corresponds to about 0.5 W power. At this simulation, the beam loss becomes larger than 1 W/m after transverse misalignment 0.85 mm.

For each quadrupole misalignment, the occurrence of the beam loss depends on the random seed of errors. Figure 8 shows the beam loss count for each quadrupole misalignment per 100 random seeds. After a quadrupole misalignment of 0.8 mm, the beam loss count increases rapidly.

The location of the beam loss occurrence along the beamline is also an important issue to correct the distorted beam orbit. Figure 9 shows the number of lost particles along the BIS beamline for a quadrupole transverse misalignment of 1.0 mm. The beam loss occurs mainly at the end of the bending section, therefore the

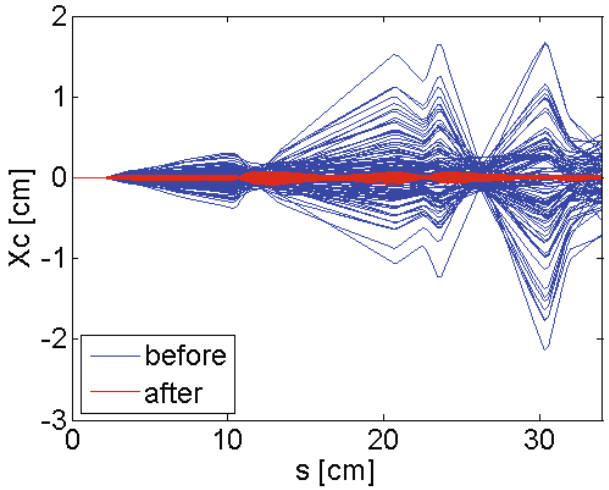


Fig. 10. Horizontal beam centroids before and after the orbit correction for the quadrupole transverse misalignment of 1.0 mm along the BIS beamline.

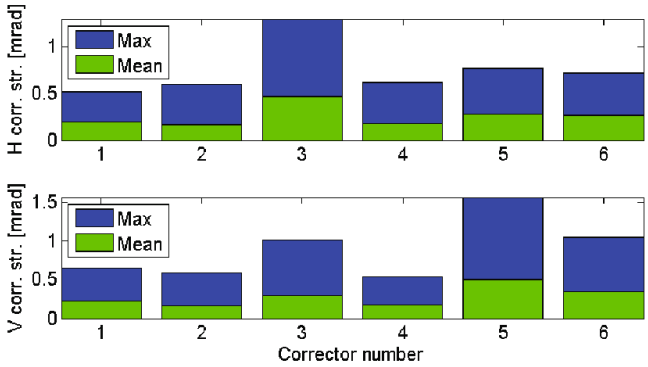


Fig. 11. Steering magnet strength for the transverse quadrupole misalignment of 1.0 mm at the BIS beamline.

orbit correction should be carried out more carefully at this section.

Although weaker than the quadrupole transverse misalignment, other machine errors can also affect the beam orbit and result in the beam loss. The tolerances of other such errors, including launch errors, quadrupole errors, and dipole errors are listed in Table 2. The tolerance is determined by the beam loss larger than 1 W/m at the BIS beamline. As listed in the table, the quadrupole transverse misalignment is a dominant source for orbit distortion and beam loss.

### 3. Orbit correction

The orbit correction was carried out by using six steering magnets and six BPMs, and the steering magnets and BPMs were distributed one-to-one along the BIS beamline. Figure 10 shows the horizontal orbit distortion before and after the orbit correction for a quadrupole transverse misalignment of 1.0 mm. The distorted orbit decreased dramatically, and the calculated kick angle of the steering magnets used at this time is shown in Fig. 11. For the carbon beam after the SCL2, the maximum kick angle of the steering magnets under consideration is about 1.0 mrad. Therefore, the distorted orbit caused by quadrupole transverse misalignments less than 1.0 mm can be corrected by using the steering magnets.

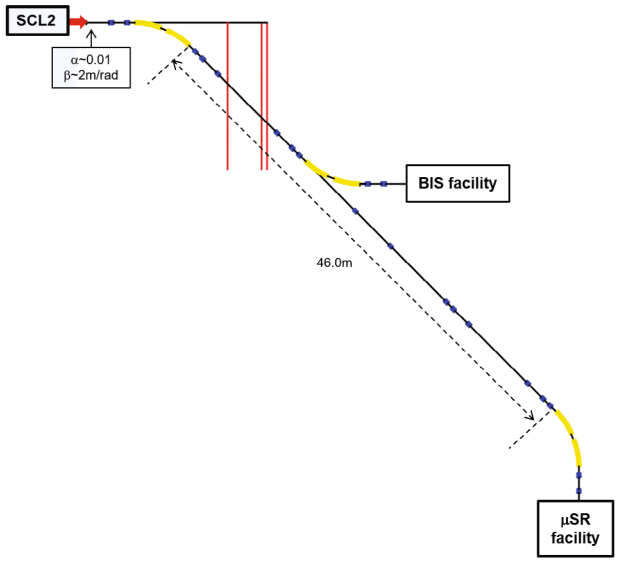


Fig. 12. Layout of the muSR beamline.

Table 3. Proton beam parameters for the muSR beamline simulations.

| Characteristic | Value | Unit |
|---|---|---|
| Energy | 623 | MeV |
| Magnetic rigidity | 4.2 | Tm |
| Velocity in unit of c | 0.801 | - |
| $\varepsilon_{x,rms,norm.}$ | 0.13 | mm.mrad |
| $\varepsilon_{y,rms,norm.}$ | 0.13 | mm.mrad |
| $\beta_{x,y,0}$ | 2.0 | m |
| $\alpha_{x,y,0}$ | 0.01 | - |
| Energy spread | 0.3 | % |
| Beam distribution | 6D water-bag | - |
| Number of macro-particles | 400k | - |

## III. MUSR BEAMLINE

### 1. Beam dynamics simulation

The layout of the muSR beamline is shown in Fig. 12. There are 18 quadrupoles and 4 dipoles, and the lattice has also been designed with the mirror symmetry condition. Like the BIS beamline, the beam pipe size has also

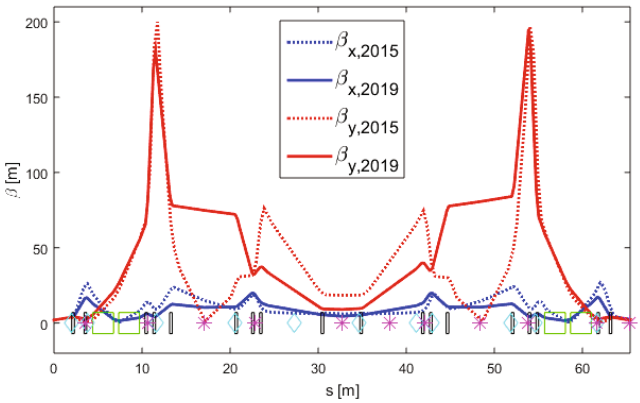


Fig. 13. Beta functions along the muSR beamline. In the figure, a green box, a black box, a cyan diamond, and a magenta star mean a dipole, a quadrupole, a corrector, and a BPM, respectively.

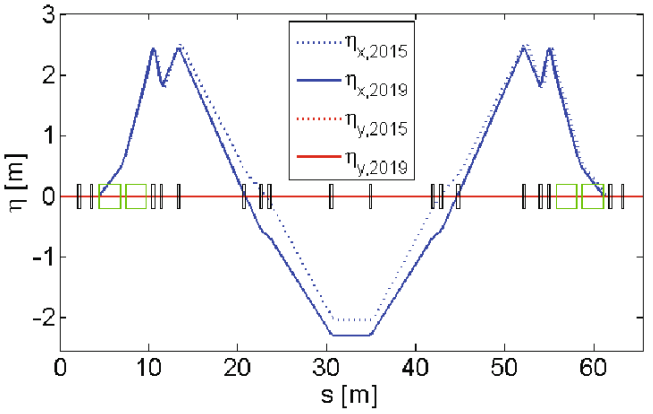


Fig. 14. Dispersion functions along the muSR beamline.

been adjusted from 4.0 cm to 3.2 cm, and the beam optics calculation is required newly. The proton is used as a reference beam at the muSR beamline, and the beam parameters used at simulations are listed in Table 3.

Figure 13 shows the beta functions along the muSR beamline. Compared to the results in 2015, the maximum horizontal and vertical beta functions are reduced slightly by adjusting the quadrupole strength.

As satisfying the achromatic condition, the dispersion functions are also calculated as shown in Fig. 14. The maximum value of the horizontal dispersion is decreased slightly, and the vertical one is kept at zero to satisfy the achromatic condition.

The particle tracking simulation was conducted by using 400,000 macro-particles. The transverse rms. beam size along the muSR beamline is shown in Fig. 15, and the transverse rms. emittance is shown in Fig. 16. The maximum value of the beam size was decreased slightly after new calculation, and the maximum value of the horizontal rms. emittance was also decreased at the dispersion section.

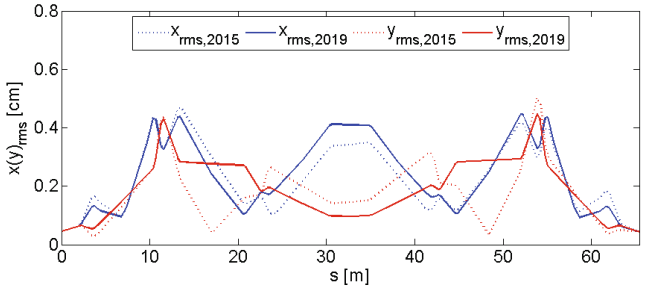


Fig. 15. Transverse rms. beam size obtained using the TRACK code at the muSR beamline.

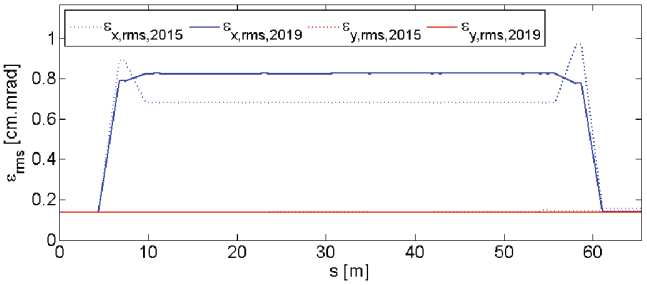


Fig. 16. Transverse rms. emittance obtained using the TRACK code at the muSR beamline.

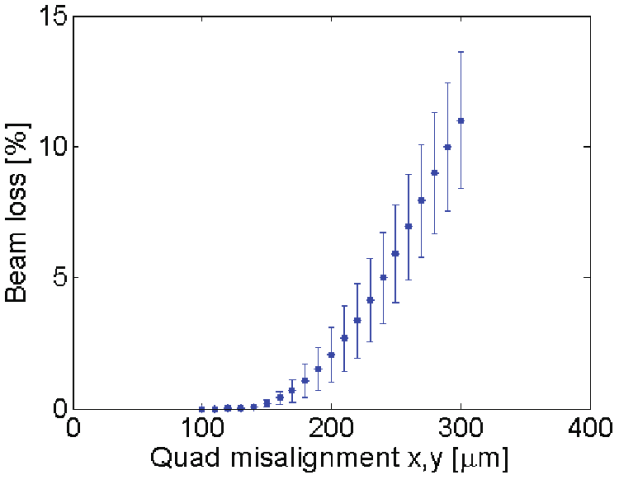


Fig. 17. Average beam loss percentage for quadrupole transverse misalignment error with 100 random seeds.

### 2. Beam loss simulation

The beam loss percentage for the quadrupole transverse misalignment with 100 random seeds is shown in Fig. 17. We used 400,000 macro-particles, and one macro-particle corresponds to a power of about 1.0 W. At this simulation, the beam loss becomes larger than 1 W/m after transverse misalignment of 120 μm, and this value is lower than the result of the BIS beamline because of the difference of the beam energy and total length of each beamline.

The beam loss count for each quadrupole misalign-

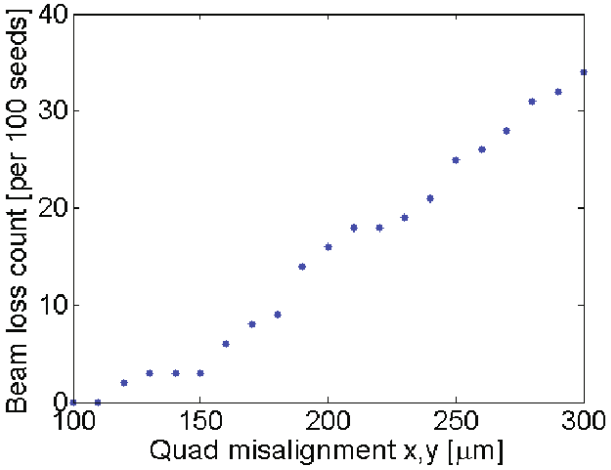


Fig. 18. Beam loss count for quadrupole transverse misalignment error per 100 random seeds.

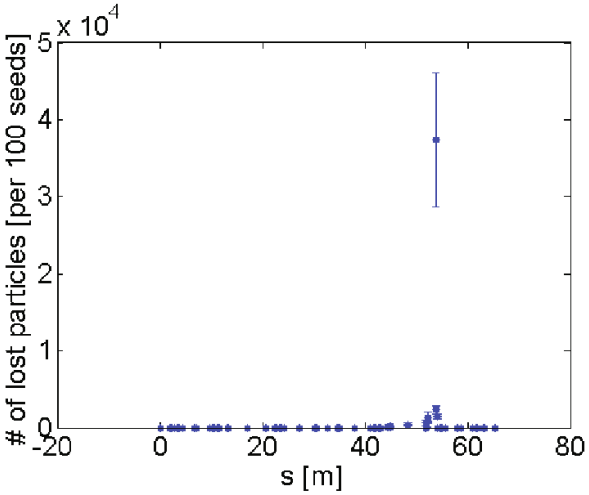


Fig. 19. Beam loss along the muSR beamline for the transverse quadrupole misalignment of 300 μm for 100 random seeds.

ment per 100 random seeds is shown in Fig. 18. After a quadrupole misalignment of 120 μm, the beam loss count increases rapidly. Therefore the orbit correction should be carried out more carefully than the case of the BIS beamline.

Figure 19 shows the number of lost particles along the muSR beamline for a quadrupole transverse misalignment of 300 μm. Most of the beam loss also occurs at the end of the bending section, therefore the orbit correction was carried out more carefully at this section.

The error tolerances at the muSR beamline are listed in Table 4. At the muSR beamline, the errors affect the beam loss more than they do for the BIS beamline because the number of magnets is larger and beamline length is longer. For that reason, the orbit correction for the muSR beamline should be carefully conducted.

Table 4. Error tolerance at the muSR beamline.

| Error tolerance | Value | Unit |
|---|---|---|
| Launch error x(y) | ±1.2 (±0.2) | cm |
| Launch error $x_p$ ($y_p$) | ±4.2 (±1.0) | mrad |
| Quadrupole misalignment x,y | ±0.11 | cm |
| Quadrupole misalignment z | ±3.3 | cm |
| Quadrupole tilt | ±1.6 | mrad |
| Dipole misalignment x,y | ±0.43 | cm |
| Dipole tilt | ±0.6 | mrad |

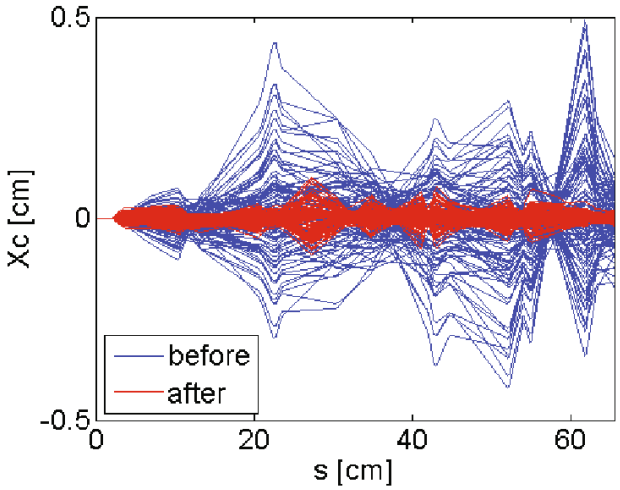


Fig. 20. Horizontal beam centroids before and after the orbit correction for the transverse quadrupole misalignment of 300 μm along the muSR beamline.

### 3. Orbit correction

Including the steering magnets and the BPMs used at the BIS beamline, the orbit correction was carried out by using the 11 steering magnets and 11 BPMs. Figure 20 shows the horizontal orbit distortion before and after the orbit correction for a quadrupole transverse misalignment of 300 μm. The distortion of the orbit was decreased after the orbit correction, and the calculated kick angles of the steering magnets used at this time, which is less than 1.0 mrad, are shown in Fig. 21. For the proton beam after the SCL2, the maximum kick angle of the steering magnets under consideration is about 1.3 mrad. The alignment of the magnets in the tunnel will be performed within 150 μm, therefore, the distorted orbit induced by the errors can be corrected by using the steering magnets and the BPMs.

## IV. CONCLUSION

We have presented the simulation results for the beam optics calculation and the beam dynamics with new

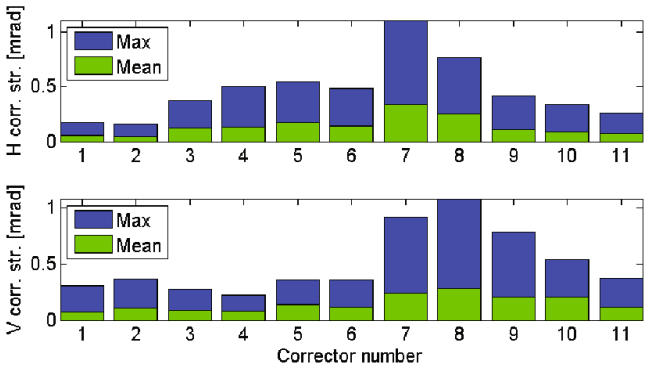


Fig. 21. Steering magnet strength for the transverse quadrupole misalignment of 300 μm at the muSR beamline.

quadrupole specifications at the BIS beamline and the muSR beamline. As the quadrupole pipe size decreases, the beta functions and the dispersion functions were calculated to keep the beam size small, after which the particle tracking simulations were conducted for verification. After these simulations, beam loss studies were carried out carefully for the quadrupole transverse misalignment, which is the dominant source of orbit distortion, and orbit corrections were also made using steering magnets and BPMs at each beamline. After the orbit corrections, the beam loss was seen to have disappeared upto the quadrupole misalignments of 1.0 mm at the BIS beamline and of 300 μm at the muSR beamline, respectively, within the maximum kick angle of the steering magnet. The tolerances of the other errors, like quadrupole tilt, dipole errors, *etc.*, were also verified. The research to determine the locations and the numbers of steering magnets and BPMs will continue.

## ACKNOWLEDGMENTS

This work was supported by the Rare Isotope Science Project of Institute for Basic Science funded by Ministry of Science and ICT and NRF of Korea (2013M7A1A1075764).

## REFERENCES

[1] D. Jeon *et al.*, J. Korean Phys. Soc. **55**, 7 (2014).
[2] D. Jeon *et al.*, in *Proceedings of HB2014* (East Lansing, MI, USA, November 10–14, 2014), TU04AB02.
[3] H. Jin and J. Jang, J. Korean Phys. Soc. **67**, 1328 (2015).
[4] H. Jin *et al.*, Nucl. Instrum. Methods Phys. Res. A **802**, 67 (2015).
[5] H. Jin *et al.*, J. Korean Phys. Soc. **70**, 59 (2017).
[6] M. Borland, LS-287, Argonne National Lab. (2000).
[7] V. Aseev *et al.*, in *Proceedings of PAC05* (Knoxville, Tennessee, USA, May 16–20, 2005), TPAT028.